Available online at www.sciencedirect.com
ScienceDirect
Earth and Planetary Science Letters 248 (2006) 618–637
EPSL
www.elsevier.com/locate/epsl

Influence of fO_2 and cooling rate on the kinetics and energetics of Fe-rich basalt crystallization

Julia E. Hammer *

Department Geology and Geophysics, University of Hawaii, 1680 East–West Rd., Honolulu, HI 96822, United States

Received 24 June 2005; received in revised form 7 April 2006; accepted 7 April 2006
Available online 6 June 2006
Editor: S. King

Abstract

Cooling rate and fO_2 are each varied over several orders of magnitude in a matrix of 1-atm constant-rate cooling experiments using synthetic basalt. The modes and compositions of olivine, pyroxene and titanomagnetite are sensitive to oxygen fugacity (ranging from QFM−4 to QFM+5 log units), whereas their textures respond to the degree of undercooling as modulated by cooling rate (ranging from 2.8 to 231 °C h^{-1}). Key results pertain to the trends in mineral composition, melt differentiation, and crystal texture development: (1) The degree of pyroxene compositional zoning in a given experiment increases with decreasing cooling rate. For a given cooling rate, the Ti/Al ratio and MgO crystal–melt partitioning coefficients for pyroxene are inversely correlated with fO_2, and the Mg contents of Ca-rich pyroxene and titanomagnetite increase with increasing fO_2. Both trends are inferred to result from the fO_2 control over melt Fe^{3+}/Fe^{2+} ratio. (2) Reducing conditions lead to greater crystal contents than do oxidizing conditions, yet for any given cooling rate the compositions of matrix glasses are progressively more evolved as fO_2 increases. The liquid lines of descent followed by residual melts are tholeiitic at reducing conditions and calc-alkaline at oxidizing conditions. The greater viscosities of residual liquids evolving toward silica enrichment at high fO_2 may be responsible for declining solidification efficiency with increasing fO_2. (3) Up to three distinct crystal populations of titanomagnetite, olivine, and pyroxene crystals, identified in each charge using qualitative morphologic criteria, are quantified in terms of volume fraction and the surface area per unit volume, S_v^P [mm^{-1}]. The presence of distinct populations suggests that nucleation of given mineral phases occurs episodically. The balance between thermodynamic driving force and kinetic inhibiting factors is optimized for the greatest number of pyroxene nucleation events at intermediate cooling rates. Anhedral crystals possess large surface area to volume (S_v^P) ratios, and these ratios are relatively insensitive to cooling rate. In contrast, the S_v^P ratios of euhedral crystal populations, as well as the weighted population averages, steadily decline with decreasing cooling rate. These trends are consistent with the energetics of 2D and 3D nucleation processes.

Keywords: crystal nucleation; crystal growth; experimental petrology; basalt; kinetics; viscosity

1. Introduction

Martian materials brought to Earth as meteorites provide valuable sources of information about planetary differentiation and magmatic processes as they occur on Mars. Studies of these meteorites have placed constraints on the nature and timing of planetary differentiation [e.g., 1], the existence of a magnetic dynamo [2,3], the composition of the mantle [4–6], the pressure and H_2O content during crystallization [7–9], and modes of magma emplacement [10]. The reconstructed

* Tel.: +1 808 956 5996; fax: +1 808 956 5512.
E-mail address: jhammer@hawaii.edu.

0012-821X/$ - see front matter © 2006 Elsevier B.V. All rights reserved.
doi:10.1016/j.epsl.2006.04.022

compositions of silicate melts represented by these meteorites point to heterogeneous mantle source regions [11]. However, they are generally distinguished from terrestrial MORB in displaying systematic compositional characteristics, such as high Fe/Al and high Fe/(Fe+Mg), that are consistent with the generally Fe-rich character of the planet [12]. An anticipated consequence of these general features is marked sensitivity of the crystallizing assemblage and liquid lines of descent to ambient oxygen fugacity (fO_2).

Crystallization experiments using synthetic Fe-rich, Al-poor basaltic starting materials have sought to relate textures and mineral compositions to undercooling and cooling rate. One approach is to target chemical or textural features of a particular meteorite and tailor experiments to constrain the conditions required to create them [10,13]. Other techniques involve modeling the subsolidus major element homogenization of olivine by diffusive transfer [14,15] and lamellae growth in pyroxene [16] in natural samples. Results indicate that cooling rates relevant to the late-stage igneous history of SNC meteorites are 0.02–5 °C h^{-1}. Recognizing the advantages of achieving a broad understanding of texture-controlling crystallization processes in meteorites, this experimental study approaches the topic somewhat differently. Cooling rate and oxygen fugacity are varied independently over several orders of magnitude to investigate the effects of intensive and kinetic factors on the liquid lines of descent, major element partitioning behavior, crystallization efficiency, and crystal morphologies. Rapid cooling (up to ~230 °C h^{-1}) was included to examine the consequences for magnetic properties, which are particularly sensitive to grain size [17]. It is hoped that producing this suite of synthetic samples, well-characterized magnetically, compositionally, and texturally, will (a) facilitate rapid comparative analysis of existing and as yet undiscovered SNC meteorites, (b) enable interpretation of magmatic processes within the framework of solidification theories, and (c) constrain thermal models of igneous bodies that may be associated with intense remanent magnetization features in the ancient southern highland terrain [18].

The composition of the starting material (Table 1) broadly resembles melts coexisting with natural olivine and pyroxene during crystallization of the SNC meteorites [7,19,20]. Insofar as its Fe-rich character is germane to a variety of inferred Martian magmas, the results are relevant to a range of possible crustal components. In addition to petrology, characterization of the experimental run product includes determination of magnetic hysteresis parameters, the amplitude and stability of remanence, and temperature-dependent order/disorder transitions. These properties are pertinent to the discussion of intense anomalies detected by the Magnetometer experiment aboard Mars Global Surveyor [21], and the results are presented separately [61]. Here we describe the phase compositions and textures of the experimental products, relate these trends to kinetic theory and the energetics of solidification, and discuss how these trends may be applied to the interpretation of natural materials.

Table 1
Compositions of synthetic starting material used in this study and several Martian meteorites

	Starting material[a]	A*[b]	QUE[c]	Eg[d]	Zagami[e]
SiO_2	51.4 (0.8)	51.5	47.7	49.0	51.2
TiO_2	1.63 (0.09)	1.58	1.92	1.70	0.81
Al_2O_3	9.13 (0.33)	8.72	10.14	7.40	6.19
FeOT	18.9 (0.5)	19.0	19.6	18.4	18.2
MgO	7.27 (0.19)	7.08	6.33	11.50	10.40
CaO	8.77 (0.21)	8.49	11.18	9.20	10.70
Na_2O	2.13 (0.09)	2.29	1.46	0.90	1.29
K_2O	0.75 (0.04)	0.77	0.05	0.00	0.13
P_2O_5	0.49 (0.05)	0.00	1.01	1.20	0.58
Total	100.4	99.5	99.4	99.3	99.5
Cation ratios					
$Fe^{2+}/(Fe^{2+}+Mg)$	0.573	0.601	0.635	0.473	0.495
Ti/Al	0.115	0.116	0.121	0.147	0.083
Fe^{2+}/Al	1.42	1.55	1.37	1.76	2.09

[a] Glass composition of fusion MA13 (see Table 2); average of 9 analyses. Values in parentheses are 1σ in oxide wt.%.
[b] Calculated melt in equilibrium with Chassigny phase assemblage [7].
[c] [58].
[d] [59].
[e] [60].

2. Methods

2.1. Experimental methods

Basalt of Chassigny A* [7] composition was synthesized from powdered oxide, carbonate, and phosphate reagents (Table 1). The mixture was heated in a controlled fO_2 atmosphere using an H_2–CO_2 flowing gas mixture to impart an intrinsic fO_2 equivalent to the desired oxygen buffer assemblage at run conditions. This pre-conditioning reduces the need for large capacity oxygen buffering during the cooling experiments. Three hundred milligrams of prepared silicate powder was placed in Mo foil or Pt capsules, and sealed inside evacuated SiO_2 glass tubes with solid-media fO_2 monitors (Appendix F1). In order of

increasing relative oxygen fugacity, the monitors are Fe° wire (IW, equal to QFM−3.4 log units), SiO_2 chips +Fa_2SiO_4 and Fe_3O_4 powders (QFM), Ni° wire+NiO powder (NNO, QFM+0.8), and MnO+Mn_3O_4 powders (MNO, QFM+5). The presence of the fO_2 monitoring components was verified at the end of the run. Limited oxygen exchange between the monitoring components and silicate is apparent in some runs by the altered proportions of the monitoring assemblage. Difficulty maintaining desired fO_2 was encountered in two of the QFM runs, which apparently oxidized to the Fe_3O_4–Fe_2O_3 buffer (MH, equal to QFM+6 log units) since hematite was observed within the silicate portion of the charge. It is assumed that the silica glass tubing failed in these case; these experiments are considered along with the other highly oxidizing runs.

Loss of Fe from the silicate to the Pt container is a perennial concern in high-temperature experiments. The loop technique [22], which minimizes the silicate/container mass ratio, is unsuitable here because representative splits of material are needed for petrography and magnetic characterization. Because partitioning of Fe between FePt alloy and Fe-oxides increases with decreasing fO_2 [23], Mo foil was used as a container in IW experiments [24]. A strategy for stemming iron loss to Pt is to anticipate the equilibrium quantity of Fe in the FePt alloy [23] and prepare an appropriate container material [25]. However, because Fe solubility in Pt and the rate of diffusive exchange changes with temperature [26], it is difficult to apply this technique to dynamic crystallization experiments. Mitigating strategies employed here include preparing the Pt capsules by first running the capsules with synthetic A* basalt for 5 h at 1200 °C (after [27]), and reusing "seasoned" capsules for several runs at the same fO_2. The relatively short total experiment durations, and particularly the short durations at high temperature (e.g., >900 °C) limit iron loss; the diffusion coefficient for Fe in Pt drops by more than two orders of magnitude between 1200 and 900 °C [28]. Of the 20 dynamic cooling experiments performed, 15 used Pt capsule materials, 8 of these are in the fO_2 range (QFM and NNO) where Fe loss may be significant, and four have cooling durations above 900 °C exceeding five hours. Strong compositional gradients in all phases preclude a mass-balance approach to evaluating the problem [e.g., 29], and direct analysis of capsule material is not possible since the capsules are reused. Given the high Fe content of the starting material, extreme losses may be required to modify the stabilities of liquidus phases. This does not appear to have occurred. Ferromagnesian silicates or Fe–Ti oxides are the dominant minerals in every charge, forming before felsic silicates. The four experiments most susceptible to iron loss (MA25, MA39, MA40, and MA49) all contain Fe–Ti oxides in abundances exceeding those of the corresponding short-duration experiments. Ferromagnesian silicates are among the most Fe-rich of the entire suite of runs. These observations suggest that iron loss has not significantly modified the compositions, modes, or textures of the experimental samples.

An S-type thermocouple housed in silica glass and linked to a digital data logger was bundled with four sample tubes (each containing a solid fO_2 buffer assemblage), heated to 1210 °C, annealed for 5 h, and then either removed from the furnace ($\sim 10^5$ °C h^{-1} quench) or cooled using a programmable temperature controller to <300 °C at one of five rates (231, 72.4, 18.7, 5.7, or 2.8 °C h^{-1}; Table 2). Splits of each run product were allocated to thin section work and characterization of magnetic properties.

Liquidus temperatures determined in quenched isothermal runs aided in selecting the initial conditions for the constant-rate cooling experiments. Ideally, the thermal histories of all cooling experiments of a given series would be identical in terms of (a) cooling time and rate, and (b) minimal superheating prior to cooling. Bundling the silica capsules and running them simultaneously ensure that condition (a) is met, because all charges experience exactly the same temperature–time history. Unfortunately, the liquidus temperature of the starting material is a strong function of fO_2. Thus, no single temperature satisfies (b), and each charge is subjected to a slightly different thermal pre-treatment relative to its liquidus temperature. An initial temperature of 1210 °C was chosen for all of the experimental runs because it is intermediate between bracketing liquidi (1205 and 1245 °C for IW and MNO, respectively). The initial temperature is no more than 5 °C above the liquidus of any starting composition, thereby minimizing the inhibitive effects of superheating for crystallization [30,31]. The MNO runs initiated 35 °C below the saturation temperature of titanomagnetite, but above all other mineral-in temperatures. Titanomagnetite crystal textures in the MNO run products are interpreted in view of this distinction.

2.2. Analytical methods

Glass, Fe–Ti oxides, pyroxenes, and olivine were analyzed by electron probe microanalysis (EPMA) on the Cameca SX-50 at the University of Hawaii. Analytical conditions for glass included an accelerating voltage of 15 kV and 10 or 15 nA defocused beam. Na

Table 2
Phase equilibrium and constant-rate cooling experiments

Run	fO_2 buffering assemblage[a]	Actual fO_2[b]	T[c] (°C)	Duration (h)	Phases[d]
Isothermal, near-liquidus experiments					
MA-7	IW	IW	1210	24	gl
MA-18	IW	IW	1210	6.5	gl
MA-35	IW	IW	1200	25	gl
MA-22	IW	IW	1190	10	gl, pyx, ol, timt (tr.)
MA-13	MMO	MMO	1275	4.5	gl
MA-2	none	QFM-1	1187	24	gl, timt, pyx
MA-11	QFM	QFM	1210	18	gl
MA-19	QFM	QFM	1210	6.5	gl
MA-10	NNO	NNO	1210	18	gl
MA-20	NNO	NNO	1210	6.5	gl
MA-52	MNO	HM	1250	13	gl, timt
MA-16	MNO	>MNO	1240	6	gl, timt
MA-14	MNO	MNO	1224	16	gl, timt
MA-6	MNO	MNO	1210	24	gl, timt
MA-36	MNO	MNO	1200	25	gl, timt
MA-4	none	≥MNO	1187	24	gl, timt, pyx, hmil (tr.)
MA-42	MNO	MNO	1165	34	gl, timt, cpx
MA-21	MNO	HM	1210	6.5	gl, timt, hm

Run	fO_2 buffering assemblage[a]	Actual fO_2^b	T_f^c (°C)	Duration (h)	Cooling rate (°C h^{-1})	Phases
Constant-rate cooling experiments						
MA-43	IW	IW	401	3.5	231	gl, ol, cpx
MA-31	IW	IW	320	12.3	72.4	gl, ol, cpx
MA-38	IW	IW	322	47.4	18.7	gl, cpx, ol
MA-23	IW	IW	310	150	5.7	gl, aug, ol [aug, ol]
MA-47	IW	IW	391	292	2.8	[pl, timt], aug, ol
MA-44	QFM	QFM	401	3.5	231	gl, cpx, [timt]
MA-32	QFM	QFM	320	12.3	72.4	gl, cpx, ol, [timt, aug]
MA-39	QFM	QFM	322	47.4	18.7	gl, cpx, ol, timt
MA-45	NNO	NNO	401	3.5	231	gl, cpx, [timt]
MA-33	NNO	NNO	320	12.3	72.4	gl, cpx, ol, [timt]
MA-40	NNO	NNO	322	47.4	18.7	gl, cpx, timt, [aug, timt, pl?]
MA-25	NNO	NNO	310	150	5.7	[aug, pl, gl], cpx, ol, timt
MA-49	NNO	NNO	391	292	2.8	[pl, aug, timt], cpx, ol, timt
MA-46	MNO	MNO	401	3.5	231	aug, gl, timt
MA-34	MNO	MNO	320	12.3	72.4	aug, gl, timt
MA-41	MNO	≥MNO	322	47.4	18.7	gl, aug, timt–mh
MA-26	MNO	MNO	310	150	5.7	gl, cpx, timt [aug, timt]
MA-50	MNO	≥MNO	391	292	2.8	gl, cpx, timt [aug]
MA-24	QFM	HM	310	150	5.7	gl, cpx, timt–mh, tihm, [aug]
MA-48	QFM	HM	391	292	2.8	gl, aug, timt–mh, cr, tihm

[a] Buffering assemblage abbreviations: IW=Fe+FeO, QFM=SiO_2+Fe_2SiO_4+Fe_3O_4, NNO=Ni+NiO, MNO=MnO+Mn_3O_4, HM=Fe_2O_3+Fe_3O_4.

[b] Estimated equivalent fO_2 buffer based on inspection of Fe-oxide mineralogy of sample, buffering assemblage at end of run, or on the intrinsic fO_2 imparted to starting material.

[c] Near-liquidus experiments were brought to 1210 °C, held for several hours, then cooled at ~ 8 °C/h to run temperature, held for the indicated duration, then quenched. Cooling-rate experiments were held at Ti for 6 h at 1210 °C, cooled at the indicated rates to T_f, then quenched.

[d] Phases are listed in order of decreasing volumetric abundance. Phase abbreviations: gl=glass, ol=olivine, pyx=undifferentiated pyroxene, cpx=Mg-rich pigeonite core zoned to Fe, Ca-rich augite toward rim, aug=single augite crystals, timt=titanomagnetite, mh=maghemite, cr=cristobalite, tihm=titanohematite, (tr.)=trace phase, [ ]=groundmass or very fine grained crystals.

was counted first for 20 s; peak count times for other elements ranged from 30 to 60 s. Major elements were calibrated on Smithsonian natural basaltic glass standards A99 and VG-2. Mn and P were calibrated on Verma garnet and Smithsonian apatite standards, respectively. Instrument drift outside analytical precision during glass analysis was monitored by repeated analysis of standards and application of nominal correction factors. Minerals were analyzed at 15 kV with a 30 nA beam. Major elements in Fe–Ti oxides, pyroxenes, and olivine were calibrated on natural mineral standards. Reported concentrations are calculated using PAP procedures [32]. Accuracy was verified by analysis of bench standards not used in calibration, and inspection of cation and oxide weight percent totals. Major elements deviate from published values by ≤1% relative; minor and trace elements deviate by ≤10%.

Fe–Ti oxides are designated as either spinel-series titanomagnetite or rhombohedral-series titanohematite using calculated mineral formulas. Spinel mineralogy is inferred when mineral formulas calculated on 4 oxygen basis yield oxide totals ~ 100% and cation totals of 3.0 ± 0.005; rhombohedral mineralogy is inferred when mineral formulas calculated on 3 oxygen basis yield oxide totals ~ 100% and cation totals of 2.0 ± 0.005. The cation-deficient spinel maghemite is identified by oxide totals ≤100% on 4 oxygen basis and nonstoichometry; the compositions of titanomagnetite crystals that have undergone low-temperature (<350 °C) oxidation, or maghematization, plot to the right of the ulvospinel–magnetite binary join in the TiO_2–FeO–Fe_2O_3 system [33].

2.3. Textural analysis

Irregular crystal shapes and ambiguously delineated crystals pose challenges to quantitative textural characterization. As described below, it is not possible to determine the distribution of crystal sizes (CSD) in the majority of run products because individual crystals intersect the section plane multiple times. Instead, properties that encompass all the crystals of a given mineral population, such as surface area to volume ratio and volume fraction, are characterized. These descriptors provide insights into the solidification mechanisms controlling crystal number density and size in a manner that is analogous to the intercepts and slopes of log-linear size distributions [e.g., 34]. We demonstrate below how these metrics relate to the energy balance that controls solidification processes.

Sections of the experimental runs were inspected using transmitted and reflected light optical microscopy and back-scattered electron (BSE) microscopy with a JEOL J5900 at the University of Hawaii. Digital images were analyzed with Image J and Adobe Photoshop. Quantification of the microtextures included assessment of population volume fraction, ϕ, and surface area per unit volume, S_v^P [mm^{-1}]. The volume fraction of a given population is equal to the area fraction of the population in randomly oriented test planes through the sample volume [35]. Area fraction was determined by selecting the appropriate range of grayscale values and tabulating the pixels possessing values within this range as a fraction of the total number of pixels in the image. Populations possessing identical gray values were manually selected. The total interfacial area of a population per unit volume of sample, S_v^T, is equal to $2 * N_L$, where N_L is the mean number of boundary intersections per unit length of randomly-oriented test line [36]. N_L is obtained by overlaying circular test lines onto each BSE image, and then digitally marking, selecting, and tallying the points where the test lines intersect boundaries between crystals and the surrounding phases (glass or other crystals). The quantity of intersections divided by the actual length of test line yields N_L. Finally, we obtain the ratio of crystal population surface area to the volume of that population as: $S_v^P = S_v^T / \phi = 2\, N_L / \phi$.

The spectrum of crystal morphologies is summarized in BSE images of Figs. 1 and 2. The NNO experimental charges alone contain nearly the full diversity of pyroxene (Fig. 1A–C), olivine (1D–E), and titanomagnetite (1G–I) morphologies. Crystal textures formed at the most oxidizing and most reducing experimental conditions are shown in Fig. 2. Morphologies are termed "euhedral" if crystals have a small number of well-developed planar faces, dominantly concave morphologies, and few to no hopper inclusions (e.g., pyroxene in Figs. 1A and 2A, olivine in 1D, 1F, and 2F). "Anhedral" morphologies are defined as acicular, skeletal, or dendritic, typically characterized by extensive concavities (e.g., pyroxene in Figs. 1B–C, 2C–E, olivine in 1E, 1G, 2G–I). Anhedral titanomagnetite is unique in that dendritic crystals are also faceted (e.g., Fig. 1I). Euhedral and anhedral crystal populations of a given phase are quantified separately. A combined S_v^P ratio for each mineral (e.g., pyroxene) in a given charge is obtained by weighting the contribution of each morphology (e.g., Fig. 1A–C) by the length of test line that was used to characterize it. Similarly, the total volume fraction of a phase is obtained by weighting the volume fractions for each morphology by the areas of BSE images used to measure them. No distinction is made between Ca-poor pyroxene and augite in textural analysis, since they are typically intergrown.

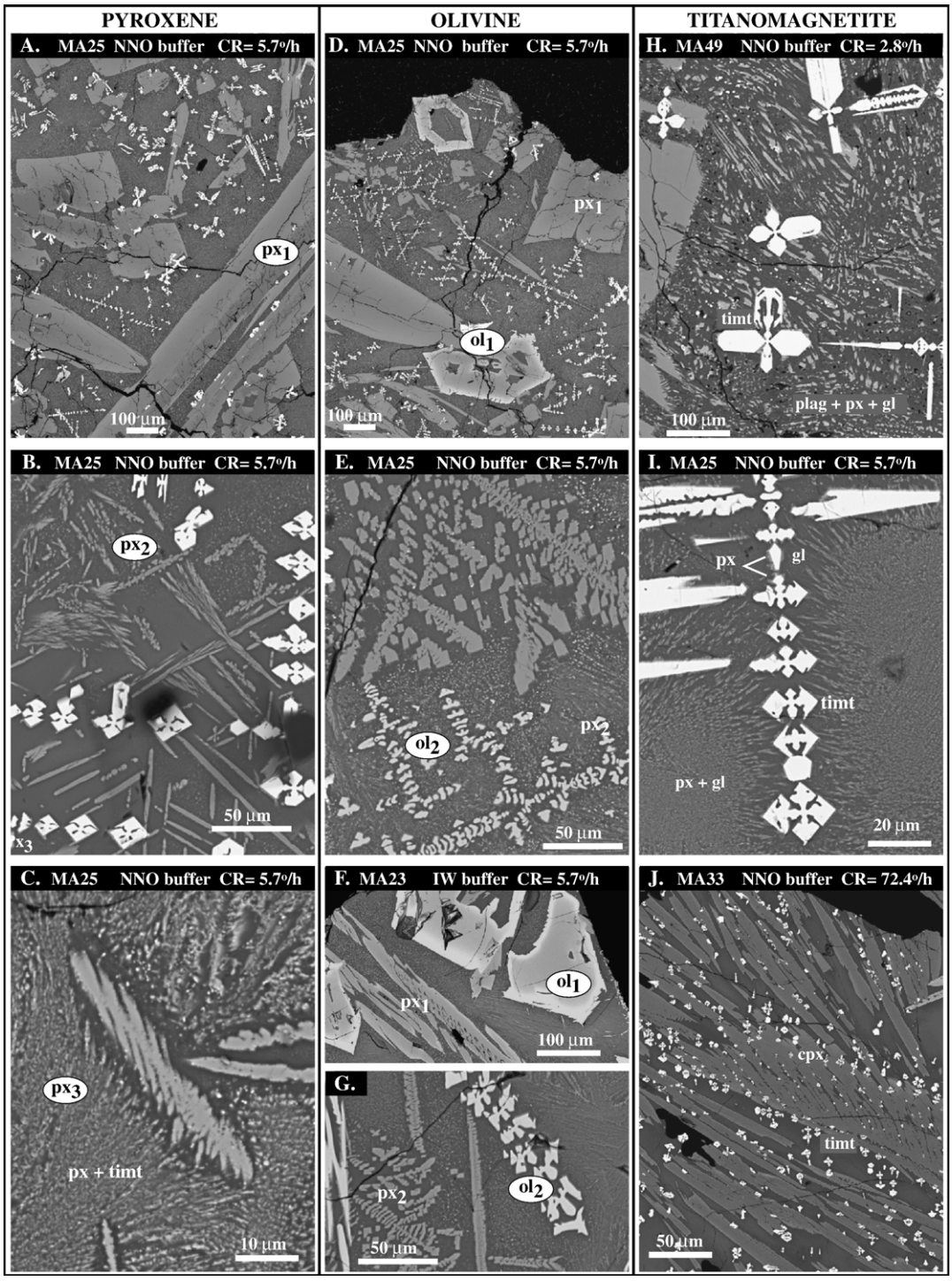

Fig. 1. Crystal morphologies characteristic of experimental pyroxene (px), olivine (ol), and titanomagnetite (timt). A single experiment at NNO/5.7 °C h^{-1} contains a population of large, zoned euhedral pyroxene (A, $\mathbf{px_1}$), a population of feathery dendritic pyroxene (B, $\mathbf{px_2}$), and a population of very fine pyroxene intergrown with titanomagnetite (C, $\mathbf{px_3}$). This experiment also contains a population of faceted, compositionally zoned hoppered olivine defined as "euhedral" (D, $\mathbf{ol_1}$) and a population of cuneiform olivine (E, $\mathbf{ol_2}$). An IW experiment at the same cooling rate contains similar olivine populations (F, $\mathbf{ol_1}$ and G, $\mathbf{ol_2}$). Titanomagnetite morphology is uniform by comparison; similar faceted dendritic crystals formed at the NNO buffer over a variety of cooling rates (H–J). Clinopyroxene coats titanomagnetite (I), and titanomagnetite grains decorate the surfaces of clinopyroxene (J). Glass and plagioclase are abbreviated "gl" and "plag".

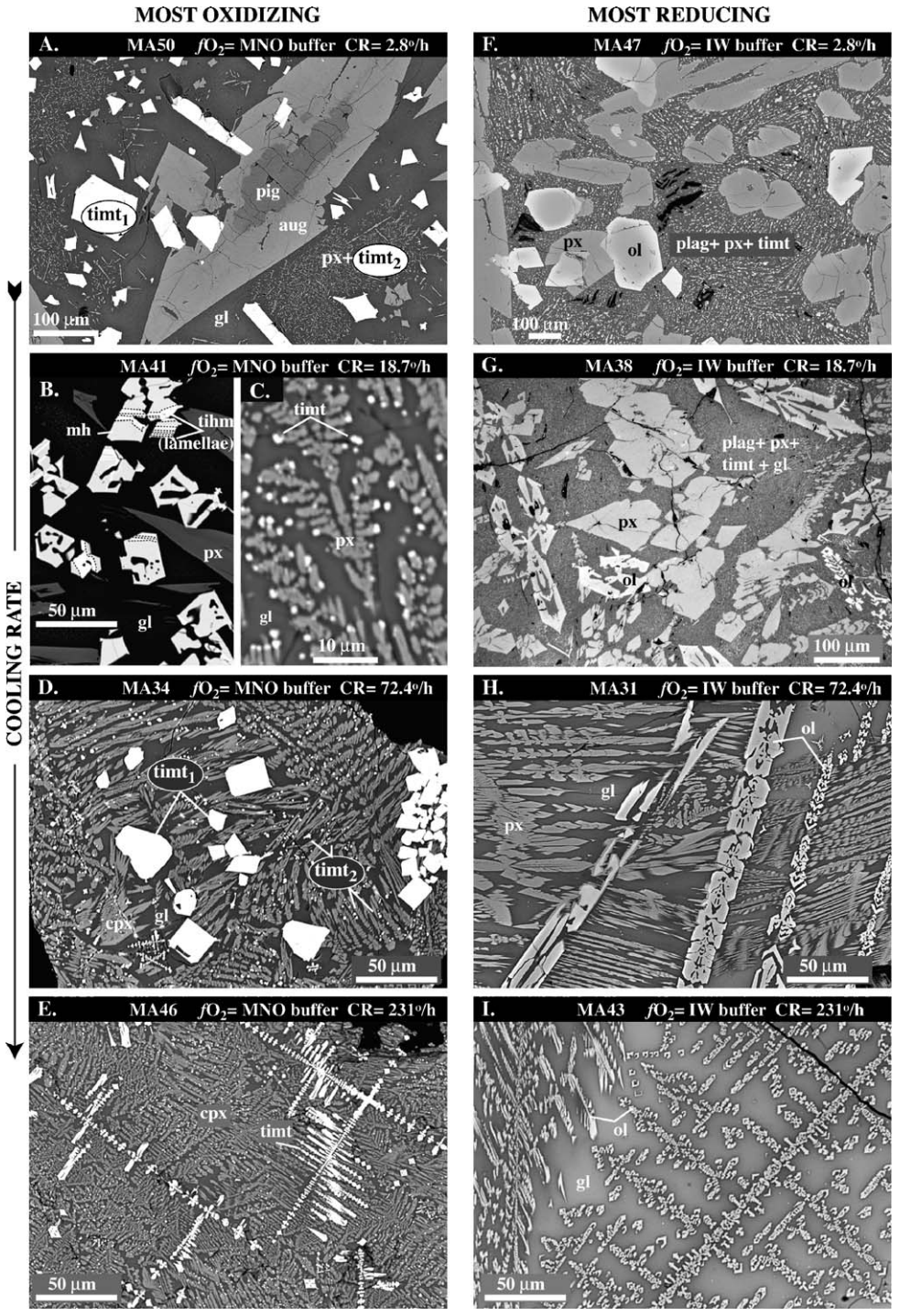

Fig. 2. Experimental textures at bracketing fO_2 conditions. Representative areas in samples cooled at the most oxidizing conditions (MNO buffer) display euhedral (**timt$_1$**) and anhedral (**timt$_2$**) populations of titanomagnetite (A), high-temperature oxidation led to titanohematite exsolution (tihm) from titanomagnetite, which subsequently underwent low-temperature oxidation to maghemite (mh) (B), dendritic pyroxene (C), two populations of titanomagnetite (D), and anhedral titanomagnetite and pyroxene populations (E). Preferential formation of titanomagnetite at the fastest-growing clinopyroxene faces, i.e., the dendrite tips (C) suggests these are sites favorable for heterogeneous titanomagnetite nucleation. A parallel set of products formed at reducing conditions (IW buffer) possess significantly greater crystallinity (e.g., F and G), with barred (H) and cuneiform (I and J) olivine. Clinopyroxene, pigeonite and augite are abbreviated “cpx”, “pig” and “aug”.

3. Results

3.1. Phase mode and composition trends

Most charges were suitable for EPMA, exceptions being feathery and dendritic crystals formed at a variety of cooling rates (e.g., Fig. 2E), and the finely crystalline groundmasses of slow-cooled runs at lower fO_2 (Figs. 1I, 2F). Representative compositions of minerals and matrix glasses are presented in Appendix Tables 1–4.

Olivine is a significant phase in the IW experiments, where it comprises up to 30 vol.% of the charges. Its abundance decreases with increasing fO_2, and it does not crystallize in any of the MNO experiments. A characteristic of euhedral olivine is pronounced normal zonation (e.g., Fig. 1F). The maximum forsterite contents of olivine cores (Fo_{65-70}) are relatively insensitive to cooling rate or fO_2. However, there is a pronounced overall trend with decreasing cooling rate toward greater compositional diversity, principally as Fe-rich phenocryst rims and microphenocrysts (Appendix T1).

Pyroxene is the dominant mineral at all fO_2 conditions. Major element pyroxene compositions are projected into the pyroxene quadrilateral in Fig. 3B. The vast majority of unzoned fine-grained crystals are ferroan augite. By contrast, phenocrysts are typically strongly zoned, having Mg-rich/Ca-poor cores and augite rims (e.g., Figs. 1A and 2A; Appendix T2). Low-Ca pyroxene cores are consistently more homogeneous than augite rims, irrespective fO_2 or cooling rate. For example, the core Mg# (En*100/(En+Fs), molecular basis) typically span a range of <5, while rims span 20–30 units. Pyroxene major element compositions vary markedly and systematically with fO_2, in contrast with the relatively fO_2-insensitive olivine compositions.

Major element pyroxene trends are also systematically related to cooling rate. Pyroxenes grown during rapid cooling are relatively uniform, ferroan augite (Mg# 61–67), while pyroxenes formed during slow cooling are more diverse (Mg# 65–86). For any given fO_2, the decreasing cooling rate is associated with increasing diversity, increasing low-Ca pyroxene abundance, and increasing Mg# of high-Ca pyroxene (particularly at highly oxidizing conditions, MNO). Low-Ca pyroxene appears in moderate to slow-cooled runs, with the cooling rate-dependence on its formation most pronounced at high fO_2.

An ilmenite-rich rhombohedral phase is not detected in any of the charges, presumably because of low concentrations of TiO_2 in the starting material. The dominant Fe–Ti oxide phase in all the runs is magnetite-rich titanomagnetite (Fig. 4, Appendix T3), and its abundance varies proportionately with fO_2. At IW, titanomagnetite appears as a minor, very late-appearing phase, while at MNO it is the first phase on the liquidus. The high magnesioferrite content of titanomagnetite

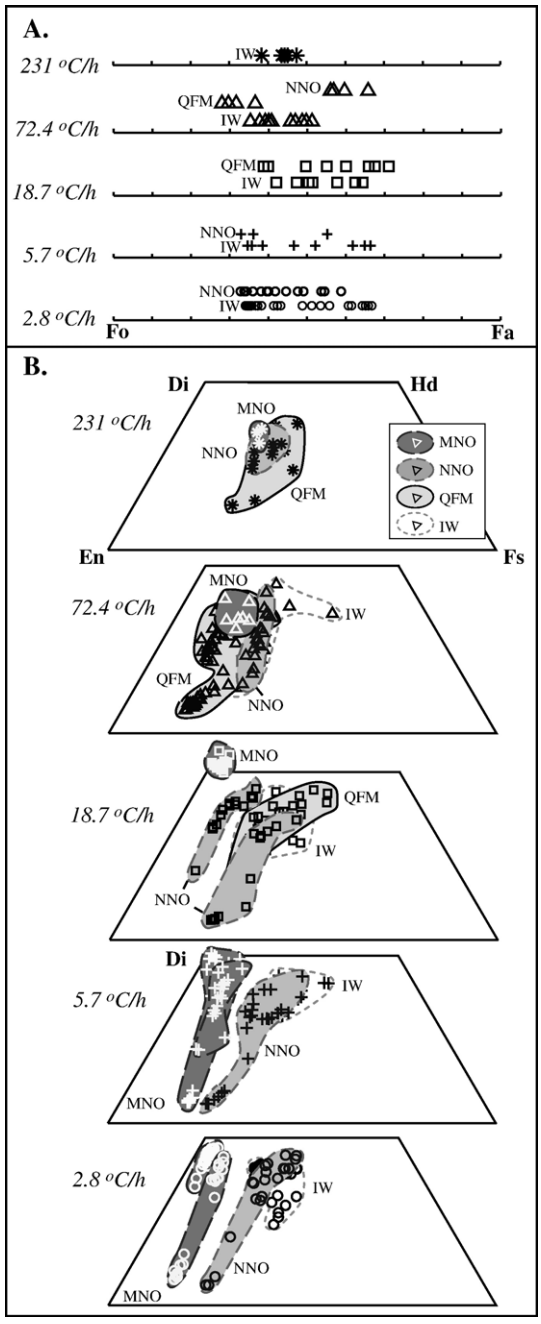

Fig. 3. Major element experimental olivine (A) and pyroxene (B) compositions. Pyroxene analyses represent single crystals (if <30 um diameter) as well as points along core-rim traverses across phenocrysts. Analyses plotting in the "forbidden zone" of the quadrilateral are inferred to reflect specimen interaction volumes that straddle a pigeonite–augite boundary.

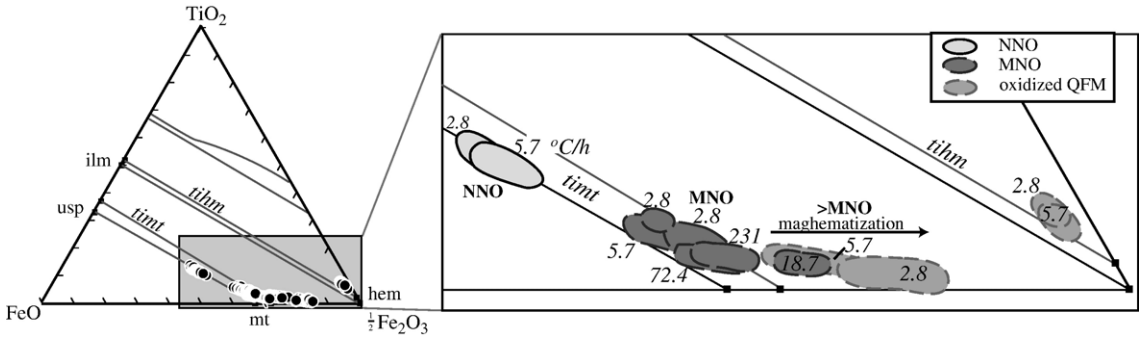

Fig. 4. Fe–Ti oxides in the system FeO–TiO_2–Fe_2O_3. Highly oxidizing conditions cause maghematization of titanomagnetite and departure from the ulvospinel (usp)–magnetite (mt) tie line. Two slow-cooled runs ostensibly held at the QFM buffer were evidently compromised, as indicated by the presence of rhombohedral Fe_2O_3-rich titanohematite (tihm) near the end-member hematite (hem) composition. These two experiments are excluded from discussion of other QFM experiments.

formed at high fO_2 (Fig. 5) parallels the high Mg# of pyroxenes at the same conditions (Fig. 3B). The limited data available to evaluate the importance of cooling rate for titanomagnetite compositions come mainly from the MNO experiments, which show slight ulvospinel enrichment as cooling rate decreases (Fig. 4).

Incipient maghematization is inferred to have altered primary titanomagnetite in several of the experiments, including two of the QFM runs (MA24 and MA48) and one at MNO (MA41). Maghematized titanomagnetite is poorer in Ti and richer in Mg than the unaltered titanomagnetite with which it occurs in irregular, banded intergrowths (Figs. 2B and 5). Hematite-rich titanohematite is also intergrown with incipiently maghematized titanomagnetite in these experiments.

In general, slow-cooled charges are more crystalline than rapidly-cooled charges run at the same fO_2, but the

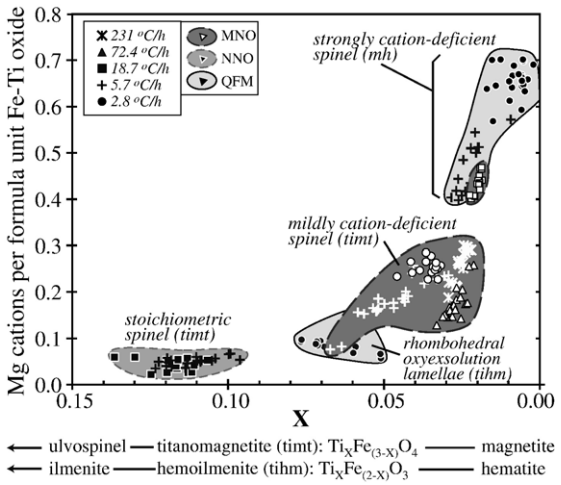

Fig. 5. Mg concentration in experimental Fe–Ti oxides. Spinel and rhombohedral oxides are increasingly magnesian as major element compositions approach Fe end-member compositions. Maghematized spinel (mh), presumably formed during low-temperature oxidation, is richer in Mg than coexisting rhombohedral titanohematite (tihm) lamellae formed during high-temperature oxyexsolution.

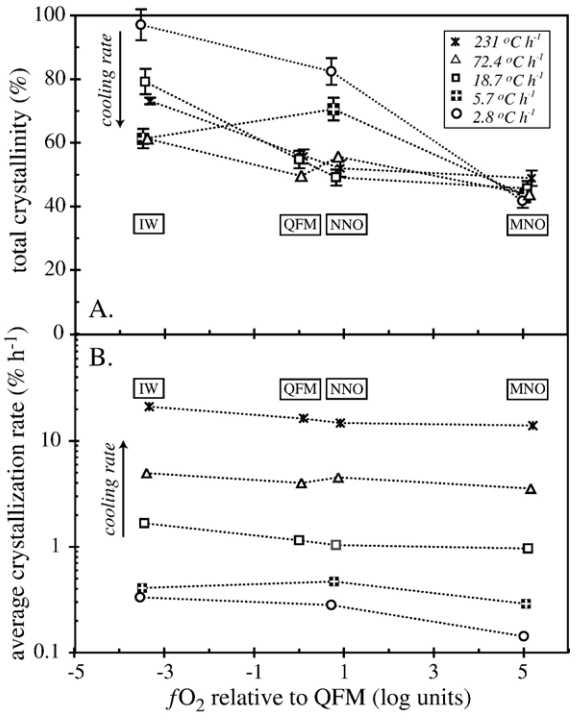

Fig. 6. Total crystallinity and integrated crystallization rate as functions of experimental fO_2. Under oxidizing conditions, total crystallinity is insensitive to cooling rate (A), reaching ~ 50% in each case. At lower fO_2, the amount crystallized generally increases with decreasing cooling rate, such that the greatest crystallization occurs in the slowest-cooled experiments. The total crystal content divided by total experiment duration yields an integrated average crystallization rate (B), which is broadly anticorrelated with fO_2. Uncertainty in rates is approximately the symbol size.

influence of cooling rate on total crystallinity appears to depend on fO_2. That is, at high fO_2 cooling rate has virtually no effect on the degree of solidification, whereas at low fO_2 there is 50% increase in crystal content as cooling rate decreases from 231 to 2.8 °C h^{-1} (Fig. 6A). For any given fO_2, crystallization during rapid cooling is dramatically faster than during slow cooling (Fig. 6B).

Samples cooled at a given rate but at different fO_2 exhibit striking differences in overall crystallinity. For example, the groundmasses of the slowest-cooled IW and MNO experiments are 90 and 49 vol.% crystalline, respectively (Table 3, Fig. 2A and F). The compositions of matrix glasses in oxidizing experiments are more evolved (higher in silica) than the matrix glasses in reducing experiments (Fig. 7), despite the fact that the former are less crystalline than the latter (Appendix T4).

3.2. Texture quantification

Cooling rate exerts the primary control on the morphologies of the three phases quantified (e.g., Fig. 2). Charges cooled ≤18.7 °C h^{-1} contain a population of euhedral olivine crystals and a second population of anhedral olivine crystals (Fig. 1D–G). In cases where multiple populations exist, they are termed "primary" and "secondary", in reference to the apparent order of appearance and not modal abundance. Runs cooled more rapidly than 18.7 °C h^{-1} contain solely the anhedral morphology (e.g., Fig. 2H–I). Three distinct populations of pyroxene, one euhedral (primary) and two anhedral (secondary and tertiary), formed in several experiments at moderate cooling rate (e.g., Fig. 1A–C). The pattern for titanomagnetite differs in that only the MNO charges contain near-equant titanomagnetite crystals (present prior to cooling) as well as a second population of cruciform and branching anhedral crystals (Fig. 2A–D). Runs at lower fO_2 contain just anhedral titanomagnetite (e.g., Fig. 1H–J).

Quantitative textural results for each population are presented in Fig. 8. In accord with expectation, the surface area to volume (S_v^P) ratios of anhedral crystal populations are greater than euhedral populations by about one order of magnitude. Less obvious from Figs. 1 and 2 are that the threshold values corresponding to the distinction between anhedral and euhedral morphologies is neither constant (for a given phase), nor uniform for all phases. The pyroxene data suggest a narrow threshold range in S_v^P values (700–1000 mm^{-1}), independent of fO_2, distinguishing euhedral from anhedral morphologies. Olivine crystals of all morphologies possess relatively low S_v^P ratios, (<700 mm^{-1} except at low

Table 3
Textural characterization of experimental run products

Run	fO_2	Cooling rate (°C h^{-1})	S_v^P, surface area to volume ratio of crystal population [mm^{-1}][a]									ϕ, volume proportion (%)			
			Pyroxene			Olivine			Fe–Ti oxide			Pyroxene	Olivine	Fe–Ti oxide	ϕ, total crystallinity[b]
			Euhed.	Anhed.[c]	Total	Euhed.	Anhed.	Total	Euhed.	Anhed.	Total	Total	Total	Total	
MA-43	IW	231	–	3694	3694	–	3282	3282	–	–	–	52	20	–	72
MA-31	IW	72.4	545	1801	1265	–	809	809	–	–	–	33	29	–	61
MA-38	IW	18.7	203	1587,5055	317	321	3962	964	–	–	–	34	11	4	79
MA-23	IW	5.7	256	2641,12192	398	142	1070	147	–	–	–	29	17	–	61
MA-47	IW	2.8	147	2619	365	165	–	188	–	6818	6818	24	12	7	90
MA-44	QFM	231	793	8425	890	–	2288	2288	–	11,715	11,715	41	11	4	56
MA-32	QFM	72.4	476	2951	690	–	532	532	–	9397	14,976	44	3	2	50
MA-39	QFM	18.7	93	1565	525	–	196	196	–	1343	1343	40	10	5	55
MA-45	NNO	231	–	1959	1959	–	–	–	–	7388	7388	49	–	2	52
MA-33	NNO	72.4	169	–	169	–	273	273	–	403	403	46	4	5	56
MA-40	NNO	18.7	64	901	122	–	–	–	–	1543	1543	46	–	4	49
MA-25	NNO	5.7	71	1979,8451	7208	98	344	200	–	1308	776	33	5	9	71
MA-49	NNO	2.8	52	4575	265	149	–	149	–	1036	1036	39	4	6	82
MA-46	MNO	231	–	2244	2244	–	–	–	1841	15057	5499	43	–	6	49
MA-34	MNO	72.4	–	1633	1633	–	–	–	1258	4784	3470	38	–	6	44
MA-41	MNO	18.7	–	1114	408	–	–	–	210	6901	1086	32	–	14	46
MA-26	MNO	5.7	325	3052	360	–	–	–	432	4007	704	35	–	8	43
MA-50	MNO	2.8	75	4857	167	–	–	–	243	–	241	29	–	13	42

[a] Measurement variance is determined by comparison of values obtained from several (typically>4) BSE images. 1σ values for S_v measurements are typically 50% relative; for ϕ the standard deviations are typically±5%.
[b] Includes plagioclase.
[c] Charges containing two distinct populations of anhedral pyroxene crystals have two entries (e.g., Fig. 1B and C).

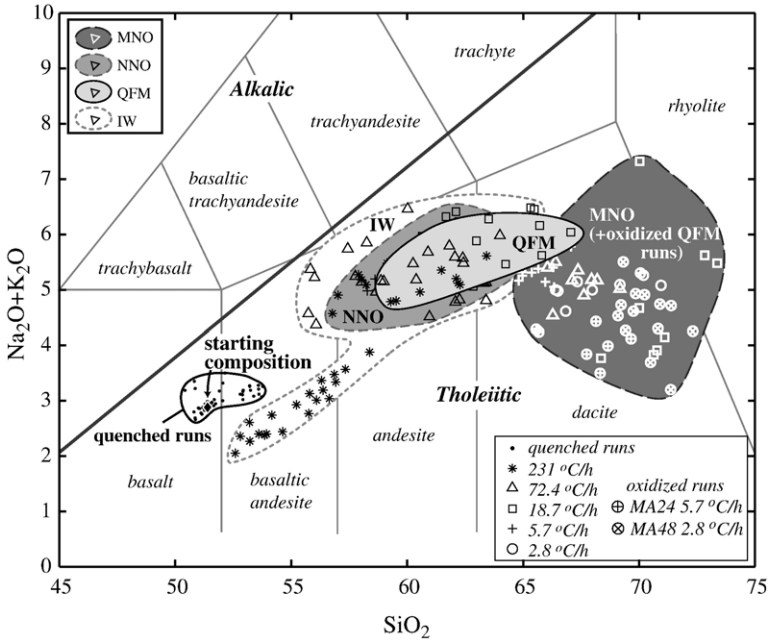

Fig. 7. Total alkali versus silica contents of experimental matrix glasses. A diverse range of compositions from individual samples indicates a high degree of glass heterogeneity. Oxidizing conditions produce silica-rich melts because crystallization of Fe–Ti oxides is modally significant. At reducing conditions, melt differentiation depends more strongly upon cooling rate, and the residual liquids are more alkalic. Crystallinity is also correlated with fO_2 and melt composition; e.g., the MNO experiment at 72.4 °C h^{-1} contains 44 vol.% crystals and dacite matrix glass, while the IW experiment at the same cooling rate contains 61 vol.% crystals and an andesitic matrix glass.

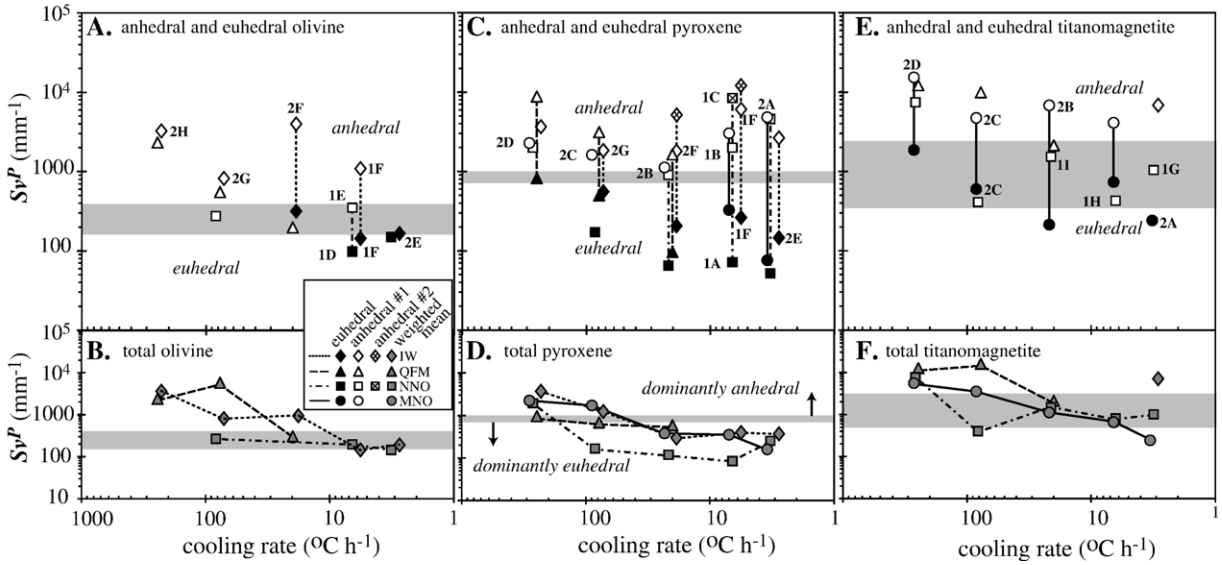

Fig. 8. Surface area to volume ratios of anhedral (open symbols) and euhedral (closed symbols) populations of olivine (A), pyroxene (C) and titanomagnetite (E). Multiple populations within the same charge are connected with a vertical patterned line. Numerals beside data points indicate a previous figure containing an image of the given population. Shaded horizontal bars represent the threshold ranges between morphologically distinct populations. Symbols representing experiments run at identical cooling rates are slightly separated along the *x*-axis for clarity. The variance in S_v^P of each population is typically ≤ 1 order of magnitude. Overall mineral ratios (B, D, F) are the combined, weighted means of all populations.

fO_2 or very rapid cooling). The threshold between morphologic groups is low (150–400 mm^{-1}) compared to pyroxene, yet not as narrow as that of pyroxene. That is, olivine crystals characterized as anhedral are not restricted to high S_v^P ratios, and euhedral crystals are not always compact. Fewer comparable data are available for titanomagnetite, but the threshold range for this mineral appears to be broader still (350–2000 mm^{-1}).

Crystal morphology has been related to the ratio G/D, where G is crystal growth rate, and D is the diffusion coefficient of crystal-forming components in the surrounding medium [37,38]. However, these experimental crystal populations display a range of morphologies including subtle variations and transitional shapes that are difficult to describe in words. The S_v^P metric may be a more appropriate indicator of the combination of these factors than morphological terminology because it is objectively quantifiable, and the surface area to volume ratio of a phase is a reflection of both the chemical driving force (partly determines G), and the development of solute-rich boundary layers (a consequence of D).

In contrast to the population ranges, the *total* values of S_v^P (weighted means of all populations) consistently decline with decreasing cooling rate, regardless of the experimental fO_2, crystallizing assemblage, mineral proportions, or mode (Fig. 8B, D, F). Furthermore, as cooling rate decreases from 231 to 3 °C h^{-1}, the overall S_v^P ratios of all three minerals decrease to <500 mm^{-1} (an exception being titanomagnetite in the groundmass of an IW experiment).

Several broad trends in the textural data are apparent. (1) The contrast between euhedral and anhedral populations slightly increases as cooling rate declines. In fact, the extrema of S_v^P ratios are exhibited by pyroxene crystals formed during slow cooling. (2) The S_v^P ratios of euhedral olivine, pyroxene, and titanomagnetite crystals consistently decrease with decreasing cooling rate. (3) When present, euhedral morphologies dominate the volumetric proportions of a given mineral, and weighted overall S_v^P values parallel the trends of the euhedral crystals. These features, exemplified by pyroxene, are depicted schematically in Fig. 9.

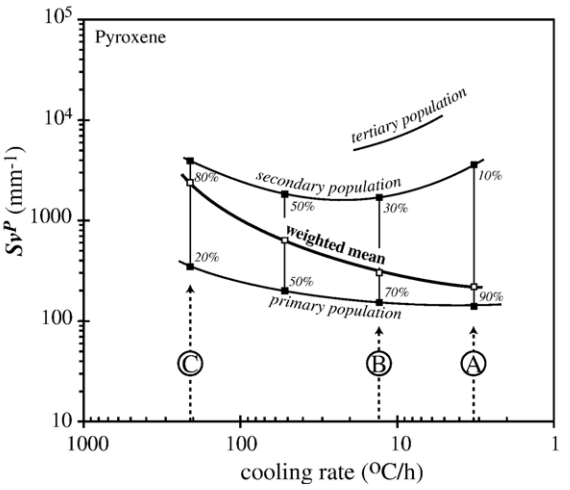

Fig. 9. Changing proportions of pyroxene populations with cooling rate. Curves are drawn schematically through all pyroxene S_v^P data (Fig. 8C and D) to illustrate that the lever rule may be applied to estimate the cooling rate from pyroxene texture of an unknown sample. The variance in S_v^P of each population is typically ≤1 order of magnitude. Although the S_v^P ratios of euhedral and anhedral populations are relatively stable, the proportional contributions to the overall texture varies continuously as a function of cooling rate. Crystallization at cooling rates corresponding to points A, B, and C are discussed in text.

4. Discussion

In the following sections we discuss the underlying causes for systematic trends in major element compositions, phase modes, and distributions of morphologies arise during cooling of Fe-rich basalt as fO_2 and cooling rate are varied. First, kinetic and compositional controls on variations in minor element partitioning in pyroxene are described. Next, inferences about fO_2 control over the liquid lines of descent (LLD), and controls on the efficiency of solidification are presented. The quantity and timing of discrete crystal nucleation events are then evaluated in view of the classical theory of crystal nucleation. Finally, S_v^P and ϕ are linked to an energy balance governing nucleation processes. We conclude by describing possible applications of these findings to the interpretation of natural samples.

4.1. Controls on major and minor element mineral compositions

Through its influence on the crystallizing assemblage and the LLD, oxygen fugacity exerts a primary control on the major and trace element contents of augite, low-Ca pyroxene, and titanomagnetite (Figs. 3–5). The robust trend toward increasing Mg contents of titanomagnetite and enstatite component (En) of pyroxene with increasing fO_2, presumably arises in response to melt $Fe_2O_3/(Fe_2O_3+FeO)$ ratio. Elevated ferric iron content in the melt at high fO_2 leads to En-rich pyroxene and high Mg contents of Fe–Ti oxides. Conversely, at reducing conditions X_{En} of pyroxene and Mg abundance in titanomagnetite decrease.

Previous dynamic crystallization studies have found that the partitioning of major elements (CaO, MgO, and

FeO) between pyroxene and basaltic melt is independent of cooling rate, and depends only upon the temperature at which a magma is quenched [39,40]. The present experiments allow examination of element partitioning at variable fO_2. Partitioning of MgO into augite, expressed as D_{MgO} ($D_{MgO}=X^{pyx}_{MgO}/X^{glass}_{MgO}$, where X is mole fraction), decreases by a factor of two between IW and MNO (from 21±6 to 9±2), while the corresponding D_{FeO} and D_{CaO} are unaltered (means and total variations are 1.9±0.3 and 3.0±0.4, respectively). The trend in D_{MgO} appears to conflict with the observation that pyroxenes are increasingly En-rich with increasing fO_2. However, the tendency for ferric iron concentration in the melt to increase with increasing fO_2 substantially elevates X_{MgO} relative to X_{FeO} in the melt. Thus, although X^{pyx}_{MgO} increases with increasing fO_2 (Fig. 3), the even greater increase in X^{glass}_{MgO} leads to a decline in the value of D_{MgO}.

The overall ranges in Al contents of pyroxene are not sensitive to oxygen fugacity, but the Ti/Al ratio for all pyroxene formed at a given cooling rate is inversely correlated with fO_2 (Fig. 10A). In the absence of plagioclase-saturation, the Ti/Al ratio in pyroxene is controlled mainly by the melt composition and thus the mode and composition of crystallizing Fe–Ti oxides. Even though titanomagnetite forming at oxidizing conditions is relatively poor in Ti (Fig. 4), the melt is depleted in Ti compared to moderate or reducing conditions where no titanomagnetite forms. Titanomagnetite control on the Ti content of the melt leads to pyroxenes with Ti/Al ratios between 1/4 and 1/8. Plagioclase crystallization has the opposite effect on pyroxene Ti/Al ratio because it depletes the melt in Al. Pyroxene crystals with Ti/Al ratios exceeding 1/2 occur in an IW run in which plagioclase is abundant (e.g., Figs. 2, and 10A).

For a given fO_2 buffer, the trace element (Al and Ti) distributions in pyroxene respond to two factors: pyroxene growth rate (controlled by cooling rate), and the change in liquid composition caused by crystallization–differentiation. These effects can be considered separately in three of the NNO experiments (231, 72.4, and 18.7 °C h^{-1}), because the amounts crystallized and pyroxene abundances are similar. The trend in both augite and low-Ca pyroxene with decreasing cooling rate is progressive expansion of the range of Al and Ti contents at constant Ti/Al ratio (Fig. 10B). Thus, cooling rate alone appears to control the magnitude of compositional heterogeneity of growing pyroxene, such that the most rapidly grown crystals are the most uniform and slower-forming crystals are more diverse. The observations are consistent with the cooling rate dependence of incompatible trace element partitioning in olivine and pyroxene [41]; pyroxene trace element concentrations parallel their abundances in the melt.

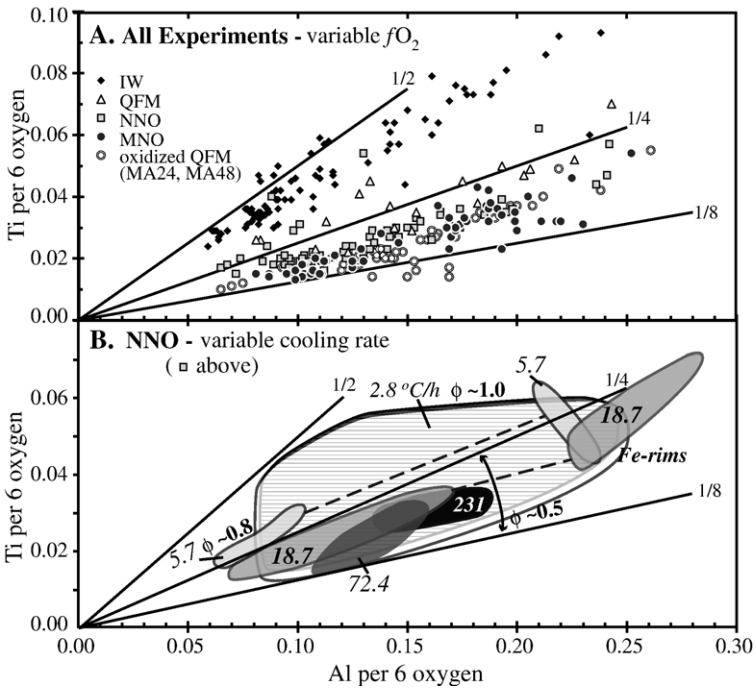

Fig. 10. Variation of Ti and Al cations per formula unit in experimental pyroxene. Taking all cooling rate data together, Ti/Al is inversely related to fO_2 (A). At a given fO_2 buffer, the diversity of pyroxene trace element abundances increases with decreasing cooling rate (B).

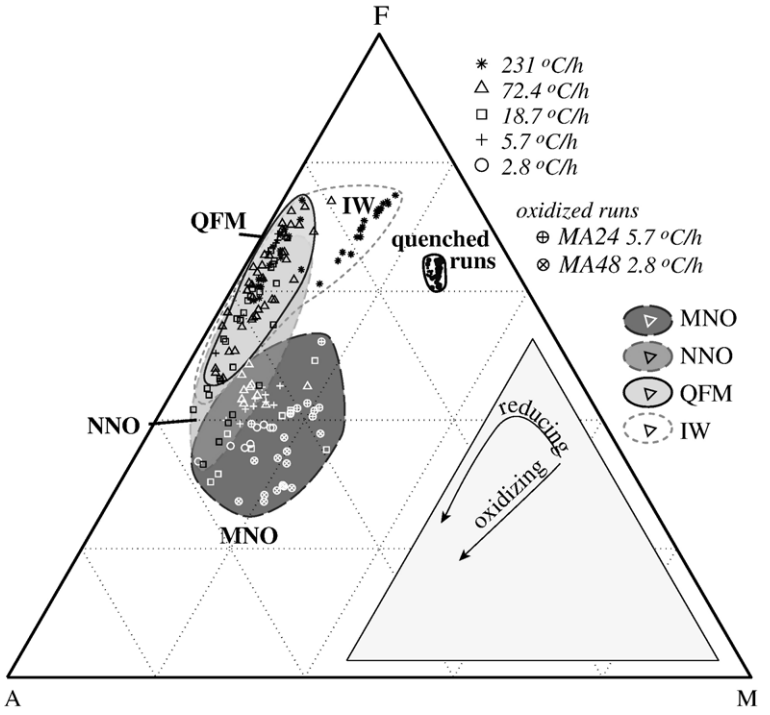

Fig. 11. Matrix glass compositions projected on an (K_2O+Na_2O)–FeO–MgO (AFM) ternary diagram. Fields enclose all experiments at a given fO_2. Inferred LLDs are shown in inset. Crystallization at reducing conditions drives residual liquids along a Fenner trend of initial Fe enrichment, while oxidizing conditions produce calc-alkaline trends.

In the NNO experiments cooled slower than 18 °C h^{-1}, plagioclase appears as a groundmass phase and Ti/Al in augite increases (Fig. 10B). In the slowest-cooled experiment (2.8 °C h^{-1}; ~80% crystalline), the trace element compositions of pyroxene are the most heterogenous. In this case, Ti/Al is controlled by the changing mode of the crystallizing assemblage. The result is a broader distribution of Ti/Al values in slow-cooled experiments, representing growth before and after plagioclase saturation.

4.2. Liquid lines of descent

Inspection of differentiation sequences among different cooling rate series on an AFM (alkalis–FeO_T–MgO) diagram (Fig. 11) suggests the following overall fO_2-control on the LLD. At low to moderate fO_2 (IW, QFM, and NNO conditions), early crystallization of Fo-rich olivine and En-rich pyroxene drives melts toward Fe-enrichment. Continued crystallization of olivine, low-Ca pyroxene, and high-Ca pyroxene causes mild alkali-enrichment and progression of the LLD along a Fenner differentiation trend. Conversely, at high fO_2, titanomagnetite crystallization leads to silica and alkali enrichment while prohibiting Fe enrichment. These findings are consistent with equilibrium experiments on basaltic systems over a range of fO_2 conditions [29,42].

4.3. Compositional controls on crystallization efficiency

That crystallization is inhibited by kinetic limitations on nucleation and growth is demonstrated by the presence of glass in all of the run products despite cooling to final temperatures (<300 °C) well below the basalt solidus (900–1020 °C, depending on fO_2). The differences in temperature at which pyroxene ceased growing may be estimated using co-existing liquid and pyroxene rim compositions. The temperature dependence of log $D_{FeO}^{\text{low-Ca pyx}}$ for quartz-normative Apollo 15 basalt cooled at low fO_2 is used to calculate closure temperatures represented by pyroxene rims in the present experiments using Eq. (2) of Grove and Bence [39].[1]

[1] The lunar basalt composition is also rich in FeO and poor in Al_2O_3, crystallizes the same assemblage upon rapid cooling. High-Ca pyroxene crystals formed in the lunar experiments were of insufficient quantity to determine the temperature dependence of FeO partitioning, and the present experiments do not allow independent determination of temperature effects. Our application of the low-Ca partitioning equation to high-Ca pyroxenes is predicated on the similarity in the slope of the log D–T relationships for high and low-Ca pyroxenes (Fig. 8 of [27]).

Calculated temperatures are highly variable, because pyroxene crystals of all sizes and morphologies are included. However, there is a consistent negative correspondence between fO_2 and pyroxene temperature. The overall ranges are 700–860 °C for IW, 670–810 °C for NNO, and 600–760 °C for MNO experiments (Appendix T2). At any given cooling rate, the temperatures are consistently ~100 °C higher at IW than at MNO. As described above, the IW charges are more crystalline than the MNO charges (Table 3). The greater crystal content of the low-fO_2 charges, despite the smaller temperature range over which crystallization apparently occurs, enhances the notion that crystallization is more efficient at low fO_2.

One explanation for these trends is that the viscosity of melts developing along a calc-alkaline trend produced at high fO_2 pose a kinetic limitation to solidification. Melt viscosity partly controls the rate at which a growing crystal face sweeps through the liquid, displacing solute. It is also implicated in classical crystallization kinetic theory as a proxy for component mobility [43]. The primary factor controlling melt viscosity in these anhydrous melts is temperature [44], yet all charges in a given series experience identical thermal histories, viscosity-influenced differences in crystallinity among them must arise from other factors. To explore the possibility of a compositional influence on viscosity and thus crystallization efficiency, the viscosities of the evolving residual melts are calculated using the MELTS algorithm [45] for bulk equilibrium crystallization at fixed fO_2 buffers (IW, QFM, NNO, and magnetite–hematite, MH). The results are shown versus fraction liquid remaining in Fig. 12. Calculated viscosities increase more steeply at oxidizing conditions because early saturation of Fe–Ti oxides induces silica enrichment of the residual liquid. Conversely, lower viscosities at moderate to reducing conditions result from greater modal silicate mineral crystallization. The difference between melt viscosities becomes particularly great as crystallinities exceed 70 vol.%. The dramatic differences in observed crystallinities exhibited by MNO (49%), NNO (82%), and IW (90%) correspond to a relatively narrow range of melt viscosities: 10^2–$10^{2.3}$ Pa s. The experimental results point to a narrow threshold in melt viscosity (~ 100–200 Pa s), above which solidification is severely inhibited during constant-rate cooling under any fO_2 conditions. Furthermore, we infer that steeply increasing melt viscosity in the early stages of crystallization at oxidizing conditions inhibits crystal nucleation (and growth) of solid phases at higher melt fraction than at moderate to

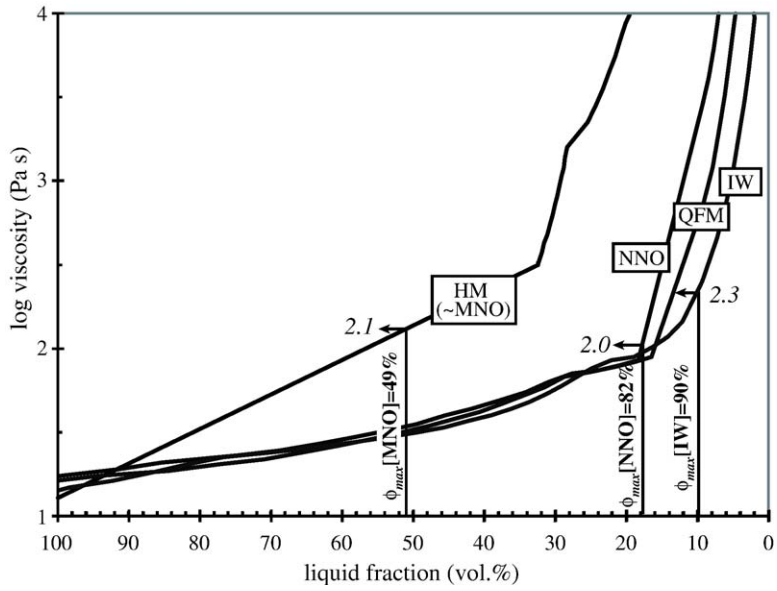

Fig. 12. Calculated viscosities of residual liquids during equilibrium crystallization at various fO_2 and maximum experimental crystal contents. Maximum crystallinity is on a volume percent basis and determined from image analysis of slowest-cooled runs at each of the three fO_2 buffers. The maximum observed crystallinities for each fO_2 are shown as vertical lines extending from the liquid fraction axis to the points of intersection with the calculated curves. The maximum crystallinity at QFM is not shown because the slowest runs at this fO_2 were compromised. The MELTS calculated temperature at which 50% crystallization occurs at IW, NNO, and MH conditions are 1088, 1094, and 1030 °C. Thus, the higher viscosity of the oxidized case is due to differences in temperature as well as residual melt composition.

reducing conditions. Oxygen fugacity apparently exerts a first-order control on the rate of solidification of otherwise identical starting materials by controlling the liquid line of descent and the rheology of derivative melts.

4.4. Crystallization kinetics and energetics

The presence of distinct crystal populations, rather than continua of morphologies and sizes, suggests that pyroxene, olivine, and titanomagnetite nucleate in discrete events. Admittedly, the evidence for discrete pyroxene nucleation is somewhat more compelling than for olivine and titanomagnetite (Fig. 8 and accompanying discussion). Experiments in which samples are progressively quenched along a cooling rate path [39,40,46] are needed to clarify this point. Classical theory states that nucleation requires a finite undercooling, or excess chemical potential driving force, to overcome the energy expenditure of forming a solid–melt interface. A simple interpretation of episodic nucleation is that it represents an unsteady response by the system to a steady change in externally applied conditions. It also implies that the activation energy barrier to nucleation is large. Crystal growth, by contrast, is most rapid at low to moderate undercoolings [47]. Compositional gradients around dendrites provide additional thermodynamic driving force, or constitutional supercooling [46,48], that may hasten nucleation of other phases. One likely example is the intimate intergrowth of pyroxene and titanomagnetite (Fig. 1J).

A satisfactory conceptual model of dynamic crystallization in these experiments should reconcile $\boldsymbol{S}_v^{\mathrm{P}}$ data and the quantity of nucleation events with crystallization theory. Textures suggest that initial undercooling, which governs the timing and vigor of the first crystal nucleation event, increases with cooling rate. Modest initial undercooling in slow-cooled charges may have led to sluggish nucleation and efficient crystal growth, delaying buildup of sufficient driving force for a secondary nucleation event. The result is that weighted mean $\boldsymbol{S}_v^{\mathrm{P}}$ values are overwhelmingly dominated by the first generation of texturally mature euhedral crystals (Fig. 9, rate A). The second nucleation event probably occurred quite late in the runs, given the high $\boldsymbol{S}_v^{\mathrm{P}}$ of anhedral crystals. In contrast, melt cooled at an intermediate rate (10–100 °C h^{-1}) is subjected to a larger degree of initial undercooling, enhancing early nucleation of first generation crystals. High temperature secondary and even tertiary nucleation events (Fig. 9, rate B) occur because the overall solidification rate is relatively rapid, owing to rapid evolution of the melt composition. Episodic nucleation is apparently optimized at these conditions. Finally, the comparative uniformity of crystal morphologies in the most rapidly cooled charges (>100 °C h^{-1}; Fig. 9, rate C) is probably due to late (low-temperature), vigorous nucleation. The textures in these runs are dominated by texturally immature, anhedral crystals.

4.5. Crystal growth affinities and forms

MAlthough external morphology of titanomagnetite varies dramatically, the dominant growth forms do not appear to shift as crystals mature. A strong crystallographic control is evident at every resolvable spatial scale and manifested as characteristic interfacial angles and distinctive cross-sectional shapes, even within the "anhedral" designation (Fig. 1H–J). A theoretical treatment of spinel bond energetics suggests a cause for the constancy of titanomagnetite forms. An interfacial energy (σ_{SL}) is required to maintain a solid–liquid interface, and an atom attachment energy (E_{a}) is released during addition of a "slice" of atoms to a given plane [49]. The octahedral {111} and rhombic–dodecahedral {110} forms represent the planes of lowest interfacial energy in spinel [50], and are predicted to dominate the equilibrium crystal morphology for this reason [51]. Forward calculation of spinel mineral *growth* forms using Hartman–Perdok analysis, which identifies periodic chains of strong bonds, predicts that the faces which evolve to prominence are those which contain two such chains and have large E_{a}. For the FCC titanomagnetite lattice, these correspond to the {111} and {110} forms. Thus, the equilibrium forms and the growth forms of spinel are identical because faces having large E_{a} also have low σ_{SL}. Periodic bond chain analysis of augite [52] indicates that {110}, {010}, and {100} have the largest E_{a} and thus are the theoretical growth forms. Unfortunately, interfacial energies of these forms are as yet unknown. A changing set of dominant forms during textural maturation of pyroxene (e.g., Fig. 1A–C), and to a lesser extent olivine, suggests that attachment energies and surface energies of these minerals are not perfectly anti-correlated.

4.6. Interfacial energy minimization

Declines in total $\boldsymbol{S}_v^{\mathrm{P}}$ for olivine, pyroxene, and titanomagnetite (Fig. 8B, D, E) with decreasing cooling rate are consistent with the classical concept of nucleation processes, in either three dimensions (i.e., volume nucleation) or two dimensions (i.e., layer nucleation). The free energy decrease of a system resulting from spontaneous crystallization is a combination of energy reduction proportional to the volume

transformed, offset by an energy "cost" that is proportional to the crystal–melt surface area:

$$\Delta G^{\mathrm{T}} = V_{\mathrm{S}}(G_V^{\mathrm{S}} - G_V^{\mathrm{L}}) + A_{\mathrm{SL}}\sigma_{\mathrm{SL}} \quad (1)$$

where ΔG^{T} is the total free energy reduction of spontaneous solidification, V_{S} is the volume of the solid, G_V^{S} and G_V^{L} are the free energies per unit volume of the solid and liquid, respectively, and A_{SL} is the solid–liquid interfacial area. Dividing Eq. (1) through by the volume of the system ($V_{\mathrm{S}}+V_{\mathrm{L}}$), recalling the definitions of $\boldsymbol{S}_v^{\mathbf{T}}$ as $A_{\mathrm{SL}}/(V_{\mathrm{S}}+V_{\mathrm{L}})$ and ϕ as $V_{\mathrm{S}}/(V_{\mathrm{S}}+V_{\mathrm{L}})$, and letting $\Delta G_V = G_V^{\mathrm{S}} - G_V^{\mathrm{L}}$, the volume-specific free energy change of solidification is:

$$\overline{\Delta G}^{\mathrm{T}} = \phi\Delta G_V + \boldsymbol{S}v\mathrm{T}\sigma_{\mathrm{SL}}. \quad (2)$$

Dividing Eq. (2) through by ϕ yields:

$$\frac{\overline{\Delta G}^{\mathrm{T}}}{\phi} = \Delta G_V + \boldsymbol{S}_v^{\mathrm{P}}\sigma_{\mathrm{SL}}. \quad (3)$$

The energy balance governing solidification is now expressed in terms of the two textural metrics determined in this study: $\boldsymbol{S}_v^{\mathrm{P}}$ and ϕ. Eq. (3) shows that the free energy of solidification is minimized by increasing ϕ (i.e., increased crystallization) and reducing $\boldsymbol{S}_v^{\mathrm{P}}$ ratio (morphologic maturation of crystals). The relative contributions of the bulk and surface terms to the overall free energy aren't known in this case, but the tendency for crystals to spontaneously coarsen will be strongest if σ_{SL} is large. The observed decline in overall $\boldsymbol{S}_v^{\mathrm{P}}$ ratios of pyroxene, titanomagnetite, and olivine with declining cooling rate indicate that surface energy plays an important role in the energy balance.

A consequence of Eq. (3) is that relative melt–crystal interfacial free energy values (σ_{SL}) could be estimated from $\boldsymbol{S}_v^{\mathrm{P}}$ data if the chemical affinities driving the formation of each mineral and total free energy changes are similar. If this assumption is correct, the phases with lowest effective σ_{SL} for any given ϕ should have the largest $\boldsymbol{S}_v^{\mathrm{P}}$. Following this logic, trends among the textural data suggest a stronger tendency for the silicates to conserve interfacial free energy. For example, the mean $\boldsymbol{S}_v^{\mathrm{P}}$ values among minerals in all experimental charges are: $\boldsymbol{S}_{v\,\mathrm{ol}}^{\mathrm{P}} \leq \boldsymbol{S}_{v\,\mathrm{pyx}}^{\mathrm{P}} < \boldsymbol{S}_{v\,\mathrm{timt}}^{\mathrm{P}}$, where the ratio for titanomagnetite is ~ 6× greater than either of the silicate values. In the absence of additional information, we might conclude that titanomagnetite possesses the lowest σ_{SL} value among these minerals. However, such a relationship would be difficult to reconcile with any plausible correlation between σ_{SL} and the structural or compositional similarity of these phases (e.g., [53]).

A study of forsterite, diopside, enstatite, and spinel (sensu strictu; $MgAl_2O_4$) wetting behavior in contact with basaltic melt provides relative σ_{SL} values from a sessile drop technique [54]. Anisotropic olivine and clinopyroxene exhibit wetting angles among various forms (e.g., {100}, {010}, {001}, and {110}) ranging from 2° to 24°. The spinel–melt values for these forms and the dominant {111} are comparatively uniform (35–42°), reflecting the istotropic symmetry of this mineral. In concept, the overall σ_{SL} could be determined for each mineral in the experiments as a combination of individual face energies weighted by their respective areas. The growth forms appear to be highly variable from experiment to experiment, and have not been identified. However, typical area proportions of the {100}, {010}, and {001} forms in natural augite and forsterite [55] and {111} in spinel, paired with wetting angle data for these forms [54] suggest overall σ_{SL} values for the silicates that are comparable to each other and ~ 10× *less* than the spinel σ_{SL} value. Thus, if relative silicate and spinel interfacial energies determined in the sessile drop study are similar to the minerals crystallizing here, the energy required to form a silicate-melt interface should be ~ 1 order of magnitude less than a spinel–melt interface.

The generally higher absolute values of titanomagnetite $\boldsymbol{S}_v^{\mathrm{P}}$ ratios and inferred σ_{SL} values compared to olivine and pyroxene are intriguing in light of this hypothesis, as they represent extravagant energy expenditures. The relationship among terms of Eq. (3) indicates that the initial assumption was incorrect; the driving force behind titanomagnetite crystal growth (ΔG_V) must have been very large in order for it to occur spontaneously.

4.7. Summary and applications

Silicate mineral compositions and inferred liquid lines of descent vary systematically with oxygen fugacity, while $\boldsymbol{S}_v^{\mathrm{P}}$ ratios of crystal populations vary mainly with cooling rate. Robust indicators of oxidizing conditions include abundant Ti-poor titanomagnetite, Mg-rich silicate mineral compositions, low pyroxene Ti/Al ratio, low overall crystallinity, melt differentiation along a calc-alkaline trend, and highly evolved quartz-normative matrix melts. Reducing conditions are reflected in abundant olivine, Fe-rich silicates, high pyroxene Ti/Al ratio, high overall crystallinity including groundmass plagioclase, matrix melt differentiation along a Fenner trend, and residual liquids richer in alkalis. Intermediate fO_2 conditions (QFM-NNO) exhibit trends that (predictably) lie between these end members, and may be distinguished from them chiefly by pyroxene Ti/Al and matrix glass compositions.

Although quite striking, titanomagnetite textures are not related to cooling rate in a manner that could be used to confidently estimate the cooling rate of an unknown. Euhedral and anhedral morphologies vary continuously in S_v^P and the ranges of values among samples cooled at the same rate under different fO_2 conditions are relatively large. Olivine morphologies evolve and the overall S_v^P decrease more systematically with cooling rate. Olivine texture is therefore promising as a quantitative cooling rate indicator. Pyroxene is the dominant mineral forming in Fe-rich basalt under all conditions examined. A rough estimate of cooling rate may be estimated simply from qualitative inspection of its texture. For example, the presence of a single population of anhedral crystals would suggest that the cooling rate exceeds 100 °C h^{-1}; three populations suggest rates of 5–20 °C h^{-1}; low aspect-ratio laths are prominent only at cooling rates < 5 °C h^{-1}. Characterization of multiple populations may be used in conjunction with Fig. 9 to further narrow the estimate. The weighted mean of S_v^P declines from ~2000 to ~200 mm^{-1} over the range of cooling rates examined, because the volumetric proportion of pyroxene comprising euhedral crystals increases with decreasing cooling rate. These relationships demonstrate that the qualitative assessment of cooling rate drawn solely upon inspection of crystal morphologies is supported quantitatively by lever-rule relationships among the S_v^P ratios of distinct populations.

The experimental trends described above may be used to infer the crystallization conditions of natural Fe-rich, Al-poor magma through quantification of mineral compositions and textures. An intrinsic limitation is that open system behavior, such as decoupled crystal–liquid advection, is not constrained by these experiments. Moreover, the pyroxene compositional trends demonstrate that the chemical zonation depends upon the LLD as well as cooling rate. Extensive controls on liquid evolution, such as the crystal–melt mass ratio, may need to be taken into account before attributing a zonation gradient to a particular cooling rate. The experiments are considered valid analogs for natural magmas (similar in composition) that solidify without crystal fractionation, e.g., in situ crystallization within mush zones and crystallization of erupting magmas. The experimental trends are also relevant to other bulk compositions, e.g., a cumulate pile with interstitial melt that matches the experimental starting material. If the crystals that existed prior to groundmass crystallization can be distinguished and isolated during image analysis, the S_v^P of subsidiary populations should evolve as documented here.

Textural analysis of the meteorite MIL-03346, a clinopyroxenite belonging to the Nakhlite group of Martian meteorites, is underway. A protracted near-surface cooling history at moderate to highly oxidizing conditions is inferred from phenocryst zoning patterns, groundmass phase assemblage, and high overall Fe^{3+}/Fe^{2+} [56]. The experimental trends described above relating cooling rate to the clinopyroxene texture yield estimates of cooling history. Preliminary S_v^P ratios of groundmass crystals, faceted microlites, and phenocryst rims in the meteorite are high (~8000 mm^{-1}), moderate (~1500 mm^{-1}), and low (~100 mm^{-1}), respectively [57], similar to the populations of clinopyroxene generated experimentally at 5.7 and 18.7 °C h^{-1}. These conditions are consistent with groundmass crystallization occurring extrusively. For comparison, a cooling rate of ~10 °C h^{-1} was measured at 24 cm depth in the 15 m thick Alae lava lake, Kilauea Volcano [58].

Acknowledgements

M. J. Rutherford is gratefully acknowledged for the use of the Experimental Petrology Laboratory at Brown University, helpful discussions, and an informal review. Comments from P. Shamberger and C. Brugger improved early drafts of this contribution. Formal reviews by T. Mikouchi, G. Bergantz, and an anonymous reviewer improved the manuscript substantially. Thanks to K. Ross for EPMA support. This work was supported by NASA award NAG512486 from the Mars Data Analysis Program and NASA award NNG05GL92G from the Mars Fundamental Research Program. This is SOEST publication number 6717.

Appendix. Supplementary data

Supplementary data associated with this article can be found in the online version, at doi:10.1016/j.epsl.2006.04.022.

References

[1] L.E. Borg, L.E. Nyquist, L.A. Taylor, H. Wiesmann, C.Y. Shih, Constraints on Martian differentiation processes from Rb–Sr and Sm–Nd isotopic analyses of the basaltic shergottite QUE 94201, Geochim. Cosmochim. Acta 61 (1997) 4915–4931.

[2] D.J. Stevenson, Mars' core and magnetism, Nature 412 (2001) 214–219.

[3] B.P. Weiss, H. Vali, F.J. Baudenbacher, J.L. Kirschvink, S.T. Stewart, D.L. Shuster, Records of an ancient Martian magnetic field in ALH84001, Earth Planet. Sci. Lett. 201 (2002) 449–463.

[4] M. Wadhwa, Redox state of Mars' upper mantle and crust from Eu anomalies in shergottite pyroxenes, Science 291 (2001) 1527–1530.

[5] C.D.K. Herd, The oxygen fugacity of olivine–phyric Martian basalts and the components within the mantle and crust of Mars, Meteorit. Planet. Sci. 38 (2003) 1793–1805.
[6] C.D.K. Herd, L.E. Borg, J.H. Jones, J.J. Papike, Oxygen fugacity and geochemical variations in the Martian basalts: implications for Martian basalt petrogenesis and the oxidation state of the upper mantle of Mars, Geochim. Cosmochim. Acta 66 (2002) 2025–2036.
[7] M.C. Johnson, M.J. Rutherford, P.C. Hess, Chassigny petrogenesis — melt compositions, intensive parameters, and water contents of Martian (?) magmas, Geochim. Cosmochim. Acta 55 (1991) 349–366.
[8] H.Y. McSween, R.P. Harvey, Outgassed water on Mars—constraints from melt inclusions in SNC meteorites, Science 259 (1993) 1890–1892.
[9] J.C. Danni, A.H. Holzheid, T.L. Grove, H.Y. McSween, Phase equilibria of the Shergotty meteorite: constraints on pre-eruptive water contents of Martian magmas and fractional crystallization under hydrous conditions, Meteorit. Planet. Sci. 36 (2001) 793–806.
[10] T.J. McCoy, G.E. Lofgren, Crystallization of the Zagami shergottite; an experimental study, Earth Planet. Sci. Lett. 173 (1999) 397–411.
[11] H.Y. McSween, What we have learned about Mars from SNC meteorites, Meteorit. Planet. Sci. 29 (1994) 757–779.
[12] H. Wanke, G. Dreibus, Chemical composition and accretion history of terrestrial planets, Philos. Trans. R. Soc. Lond. 325 (1988) 545–557.
[13] E. Stolper, H.Y. McSween Jr, Petrology and origin of the shergottite meteorites, Geochim. Cosmochim. Acta 43 (1979) 1475–1498.
[14] T. Mikouchi, M. Miyamoto, Mineralogy and olivine cooling rate of the Dhofar 019 shergottite, Antarct. Meteor. Res. 15 (2002) 122–142.
[15] T. Mikouchi, M. Miyamoto, M.G., Mineralogy and petrology of the Dar al Gani 476 Martian meteorite: implications for its cooling history and relationship to other shergottites, Meteorit. Planet. Sci. 36 (2001) 531–548.
[16] T.J. McCoy, G.J. Taylor, K. Keil, Zagami — product of a 2-stage magmatic history, Geochim. Cosmochim. Acta 56 (1992) 3571–3582.
[17] D.J. Dunlop, O. Ozdemir, Rock Magnetism: Fundamentals and Frontiers, Cambridge University Press, 1997.
[18] J.E.P. Connerney, M.H. Acuna, P.J. Wasilewski, G. Kletetschka, N.F. Ness, H. Reme, R.P. Lin, D.L. Mitchell, The global magnetic field of Mars and implications for crustal evolution, Geophys. Res. Lett. 28 (2001) 4015–4018.
[19] A.H. Treiman, The parent magma of the Nakhla (SNC) meteorite, inferred from magmatic inclusions, Geochim. Cosmochim. Acta 57 (1993) 4753–4767.
[20] V.P.S. Hale, H.Y. McSween, G.A. McKay, Re-evaluation of intercumulus liquid composition and oxidation state for the Shergotty meteorite, Geochim. Cosmochim. Acta 63 (1999) 1459–1470.
[21] M.H. Acuna, J.E.P. Connerney, P. Wasilewski, R.P. Lin, D. Mitchell, K.A. Anderson, C.W. Carlson, J. McFadden, H.R. Reme, C. Mazelle, D. Vignes, S.J. Bauer, P. Cloutier, N.F. Ness, Magnetic field of Mars: summary of results from the aerobraking and mapping orbits, J. Geophys. Res. 106 (2001) 23403–23417.
[22] D.C. Presnall, N.L. Brenner, A method for studying iron silicate liquids under reducing conditions with negligible iron loss, Geochim. Cosmochim. Acta 38 (1974) 1785–1788.
[23] R. Kessel, J.R. Beckett, E.M. Stolper, Thermodynamic properties of the Pt–Fe system, Am. Mineral. 86 (2001) 1003–1014.
[24] P.C. Hess, M.J. Rutherford, R.N. Guillemette, F.J. Ryerson, H.A. Tuchfeld, Residual products of fractional crystallization of lunar magmas; an experimental study, in: R.B. Merrill, N.J. Hubbard, W.W. Mendell, R.J. Williams (Eds.), 6th Lunar Science Conference, Pergamon Press, Houston, TX, 1975, pp. 895–909.
[25] T.L. Grove, Use of FePt alloys to eliminate the iron loss problem in 1 atmosphere gas mixing experiments: theoretical and practical considerations, Contrib. Mineral. Petrol. 78 (1981) 298–304.
[26] R.B. Merrill, P.J. Wyllie, Absorption of iron by platinum capsules in high pressure rock melting experiments, Am. Mineral. 58 (1973) 16–20.
[27] G. Moore, I.S.E. Carmichael, The hydrous phase equilibria (to 3 kbar) of an andesite and basaltic andesite from western Mexico: constraints on water content and conditions of phenocryst growth, Contrib. Mineral. Petrol. 130 (1998) 304–319.
[28] S.R. van der Laan, A.F. Koster van Groos, Pt–Fe alloys in experimental petrology applied to high-pressure research on Fe-bearing systems, Am. Mineral. 76 (1991) 1940–1949.
[29] T.W. Sisson, T.L. Grove, Experimental investigations of the role of H_2O in calc-alkaline differentiation and subduction zone magmatism, Contrib. Mineral. Petrol. 113 (1993) 143–166.
[30] M.J. Davis, P.D. Ihinger, Effects of thermal history on crystal nucleation in silicate melt: numerical simulations, J. Geophys. Res. 107 (2002) 2284.
[31] H. Sato, Textural difference between pahoehoe and a'a lavas of Izu-Oshima Volcano, Japan—an experimental study on population density of plagioclase, J. Volcanol. Geotherm. Res. 66 (1995) 101–113.
[32] J.L. Pouchou, F. Pichoir, A simplified version of the PAP model for matrix corrections in EPMA, in: D.E. Newbury (Ed.), Microbeam Analysis, San Francisco Press, San Francisco, 1988, pp. 315–318.
[33] D.H. Lindsley, The crystal chemistry and structure of oxide minerals as exemplified by the Fe–Ti oxides, Rev. Miner. 3 (1976) L1–L60.
[34] B.D. Marsh, Crystal size distributions (CSD) in rocks and the kinetics and dynamics of crystallization I. Theory, Contrib. Mineral. Petrol. 99 (1988) 277–291.
[35] J.E. Hilliard, Measurement of volume in volume, in: R.T. DeHoff, F.N. Rhines (Eds.), Quantitative Microscopy, . McGraw-Hill Series in Materials Science and Engineering, McGraw-Hill, New York, 1968, pp. 45–76.
[36] E.E. Underwood, Surface area and length in volume, in: R.T. DeHoff, F.N. Rhines (Eds.), Quantitative Microscopy, McGraw-Hill, New York, 1968, pp. 78–127.
[37] J.E. Hammer, M.J. Rutherford, An experimental study of the kinetics of decompression-induced crystallization in silicic melt, J. Geophys. Res., B: Solid Earth 107 (2002) 8-1–8-24.
[38] G. Lofgren, An experimental study of plagioclase crystal morphology: isothermal crystallization, Am. J. Sci. 274 (1974) 243–273.
[39] T.L. Grove, A.E. Bence, Experimental study of pyroxene–liquid interaction in quartz-normative Basalt 15597, Lunar Science Conference, vol. VIII, 1977, pp. 1549–1579.
[40] R.P. Gamble, L.A. Taylor, Crystal/liquid partitioning in augite: effects of cooling rate, Earth Planet. Sci. Lett. 47 (1980) 21–33.
[41] A.K. Kennedy, G.E. Lofgren, G.J. Wasserburg, An experimental study of trace element partitioning between olivine, orthopyroxene and melt in chondrules; equilibrium values and kinetic effects, Earth Planet. Sci. Lett. 115 (1993) 177–195.

[42] S.D. Spulber, M.J. Rutherford, The origin of rhyolite and plagiogranite in oceanic crust: an experimental study, J. Petrol. 24 (1983) 1–25.
[43] P.F. James, Kinetics of crystal nucleation in lithium silicate glasses, Phys. Chem. Glasses 15 (1974) 95–105.
[44] H. Shaw, Viscosities of magmatic silicate liquids: an empirical method of prediction, Am. J. Sci. 272 (1972) 870–889.
[45] M.S. Ghiorso, R.O. Sack, Chemical mass transfer in magmatic processes: IV. A revised and internally consistent thermodynamic model for the interpolation and extrapolation of liquid–solid equilibria in magmatic systems at elevated temperatures and pressures, Contrib. Mineral. Petrol. 119 (1995) 197–212.
[46] D. Walker, R.J. Kirkpatrick, J. Longhi, J.F. Hays, Crystallization history of lunar picritic basalt Sample 12002; phase-equilibria and cooling-rate studies, GSA Bull. 87 (1976) 646–656.
[47] R.J. Kirkpatrick, G.R. Robinson, J.F. Hays, Kinetics of crystal growth from silicate melts: anorthite and diopside, J. Geophys. Res. 81 (1976) 5715–5720.
[48] R.J. Kirkpatrick, Crystal growth from the melt; a review, Am. Mineral. 60 (1975) 798–814.
[49] P. Hartman, W.G. Perdok, On the relations between structure and morphology of crystals: I, Acta Crystallogr. 8 (1955) 49–52.
[50] R. Dekkers, C.F. Woensdregt, Crystal structure control on surface topology and crystal morphology of normal spinel ($MgAl_2O_4$), J. Cryst. Growth 236 (2002) 441–454.
[51] J.W. Gibbs, On the equilibrium of heterogeneous substances, The Scientific Papers of J. Willard Gibbs, vol. 1, Ox Bow Press, Woodbridge, 1906, pp. 55–353.
[52] M. Panhuys-Sigler, P. Hartman, Theoretical morphology of pyroxenes deduced from the crystal structure, Bull. Minéral. 104 (1981) 95–106.
[53] W. Wu, G.H. Nancollas, Determination of interfacial tension from crystallization and dissolution data: a comparison with other methods, Adv. Colloid Interface Sci. 79 (1999) 229–279.
[54] F.N. Shafer, S.F. Foley, The effect of crystal orientation on the wetting behavior of silicate melts on the surfaces of spinel peridotite minerals, Contrib. Mineral. Petrol. 143 (2002) 254–261.
[55] W.A. Deer, R.A. Howie, J. Zussman, An Introduction to the Rock-Forming Minerals, John Wiley & Sons, 1992, 696 pp.
[56] M.D. Dyar, A.H. Treiman, C.M. Pieters, T. Hiroi, M.D. Lane, V. O'Connor, MIL03346, the most oxidized Martian meteorite: a first look at spectroscopy, petrography, and mineral chemistry, J. Geophys. Res. 110 (2005).
[57] J.E. Hammer, M.J. Rutherford, Experimental crystallization of Fe-rich basalt: application to cooling rate and oxygen fugacity of Nakhlite MIL-03346, 36th Lunar and Planetary Science Conference CD-ROM, pp. abstract #1999, 2005.
[58] D.L. Peck, T.L. Wright, J.G. Moore, Crystallization of tholeiitic basalt in Alae lava lake, Hawaii, Bull. Volcanol. 29 (1966) 629–655.
[59] C.D.K. Herd, A.H. Treiman, G.A. McKay, C.K. Shearer, The behavior of Li and B during planetary basalt crystallization, Am. Mineral. 89 (2004) 832–840.
[60] C.D.K. Herd, C.S. Schwandt, J.H. Jones, J.J. Papike, An experimental and petrographic investigation of Elephant Moraine 79001 lithology A; implications for its petrogenesis and the partitioning of chromium and vanadium in a Martian basalt, Meteorit. Planet. Sci. 37 (2002) 987–1000.
[61] S.A. Brachfeld, J.E. Hammer, Rock-magnetic and remanence properties of synthetic Fe-rich basalts: implications for Mars crustal anomalies, Earth Planet. Sci. Lett. 248 (2006) 599–617 (this issue). doi:10.1016/j.epsl.2006.04.015.